Volume 1 | Number 1 | Jan 2013 | Pages 1–100

Nanoscale

www.rsc.org/nanoscale

ROYAL SOCIETY OF CHEMISTRY

ROYAL SOCIETY OF CHEMISTRY

www.rsc.org/nanoscale

Dense arrays of cobalt nanorods as rare-earth free permanent magnets†

E. Anagnostopoulou,[a] B. Grindi,[a] L.–M. Lacroix,[a] F. Ott,[b] I. Panagiotopoulos,[c] G. Viau[a,]*

a. Université de Toulouse, Laboratoire de Physique et Chimie des Nano-Objets, UMR 5215 INSA, CNRS, UPS, 135 avenue de Rangueil F-31077 Toulouse cedex 4, France

b. Laboratoire Léon Brillouin CEA/CNRS UMR12, Centre d'Etudes de Saclay, 91191 Gif sur Yvette, France

c. Department of Materials Science and Engineering, University of Ioannina, Ioannina 45110, Greece

Abstract

We demonstrate in this paper the feasibility to elaborate rare-earth free permanent magnets based on cobalt nanorods assemblies with energy product *(BH)$_{max}$* exceeding 150 kJ.m^{-3}. The cobalt rods were prepared by the polyol process and assembled from wet suspensions under a magnetic field. Magnetization loops of dense assemblies with remanence to saturation of 0.99 and squareness of 0.96 were measured. The almost perfect *M(H)* loop squareness together with electron microscopy and small angle neutron scattering demonstrate the excellent alignment of the rods within the assemblies. The magnetic volume fraction was carefully measured by coupling magnetic and thermogravimetric analysis and found in the range from 45 to 55%, depending on the rod diameter and the alignment procedure. This allowed a quantitative assessment of the *(BH)$_{max}$* values. The highest *(BH)$_{max}$* of 165 kJ.m^{-3} was obtained for a sample combining a high magnetic volume fraction and a very large *M(H)* loop squareness. This study shows that this bottom-up approach is very promising to get new hard magnetic materials that can compete in the permanent magnet panorama and fill the gap between the ferrites and the NdFeB magnets.

Introduction

Permanent magnets have become essential to daily life products. Ranging from electronic power generation to energy conversion and transportation, the domain of application of magnets is growing exponentially. This huge market is mostly trusted by rare earth-based magnets, that exhibit the best performances, and the ferrites based-magnets, that are by far the cheapest.[1] The fear of a rare-earth supply limitation has recently motivated numerous efforts on rare-earth free permanent magnets.[2,3] A reasonable objective is to find new hard magnetic materials that could fill the gap between the Ba(Sr) hexaferrites and the powerful NdFeB magnets. The first approach consists in playing with crystal structures in order to find new high magneto-crystalline compounds such as manganese compounds,[4] iron-nickel,[5] and iron-cobalt borides with tetragonal structure,[6] or cobalt carbides Co_2C/Co_3C nanocomposites.[7,8] An alternative approach consists in assembling single domain nanoparticles with high anisotropy into dense materials and to exploit nano-structuration.[9,10] This bottom-up approach has the advantage over the classical metallurgy processes to be scalable down to submillimeter sizes and could address the demand for microscale permanent magnets with high added values.[11]

Recently, several processes were developed to synthesize hard magnetic particles with a very good size control in the nanometer range. One interest of nanoparticles is that metastable and/or new structures can appear for sub 10 nm sizes. For example, Balamurugan et al. showed that intermetallic Zr_xCo_{100-x} nanoparticles prepared by cluster deposition crystallized in the high-anisotropy rhombohedral Zr_2Co_{11} structure for a broad composition range.[12] Moreover, the size control allows a fine control of the magnetic properties and enables these particles to be suitable for spring magnet elaboration.[13,14] Finally, nanoparticles with a great variety of shapes can be obtained by chemical processes offering the possibility to get nanoparticles with anisotropic shapes. This is the case of magnetic nanorods (NRs) and nanowires (NWs) the synthesis of which has been developed both by electrochemistry and wet-chemistry.[15] Liquid phase synthesis of FeCo,[16] Ni,[17] and CoNi[18] high aspect ratio particles were developed. Nevertheless, the coercivity of these compositions was limited compared to those measured on cobalt high aspect ratio particles. The great advantage of Co NWs and NRs in the field of hard magnetic material is the possibility to add magnetocrystalline and shape anisotropy. For cobalt wires with the hcp structure and the c axis parallel to the wire long axis a theoretical coercivity $\mu_0Hc = \mu_0M_S/2 + K_1/2M_S = 0.89 + 0.58 = 1.47$ T is expected provided that the Stoner-Wohlfarth model applies.

Co NWs and NRs with high coercivity were first synthesized by the polyol process[19] and organometallic chemistry.[20,21] These last few years several experimental works were devoted to Co NWs and NRs for permanent magnet applications with main objectives a better shape control and an improvement of their magnetic properties. Co NRs with enhanced coercivity, $\mu_0 H_C$ higher than 1T, were obtained by Gandha et al. thanks to a modified polyol synthesis in solvothermal conditions.[22] A detailed study of the polyol synthesis mechanism clearly identified the role of the laurate ion concentration on the growth of hcp cobalt, parallel or perpendicular to the c axis.[23] Scale-up of high aspect ratio nanoparticle synthesis by the polyol process was developed.[24] Parallel alignments of cobalt nanorods prepared by organometallic chemistry and characterized by magnetization loops with remanence to saturation ratio close to 1 were obtained by grafting liquid crystals at their surface.[25] High temperature stability of cobalt nanorods was improved by a thin carbon coating.[26,27]

Furthermore, several theoretical works were recently devoted to the magnetic properties of isolated or assembled Co NWs and NRs. The effects of the particle shape on the coercivity and on the magnetization reversal were described by micromagnetic modelling.[28] The role of the dipolar interactions in rod assemblies on the coercivity[29] and the calculation of the energy product as a function of the wire packing fraction[30,31] allowed assessing the performance of permanent magnets based on Co NR assemblies.

The last issue, that has not yet been addressed experimentally, is the elaboration of dense arrays of parallel nanorods. The easy-axis alignment is of paramount importance in order to obtain high energy product.[32,33] Nevertheless, high energy products require also high magnetic induction, namely, for rods assemblies, a high packing fraction.

In this paper we describe the elaboration of dense assemblies of Co NRs with different diameters and morphologies prepared by the polyol process. The rod alignment and the magnetic volume fraction were characterized by electron microscopy, neutrons scattering, thermal analysis and magnetic measurements. This is the first time that energy products of nanorods assemblies have been assessed. We show that the performance of these new magnetic materials makes them very good candidates to compete in the new rare-earth free permanent magnet panorama.

Experimental

Synthesis and characterization of Co NRs

Cobalt nanowires were produced by the polyol process following a procedure previously described.[19] Cobalt acetate was purchased from Alfa Aesar, sodium hydroxide, lauric acid and 1,2-butanediol from Acros, and hydrated ruthenium chloride from Sigma-Aldrich (ref. Sigma Aldrich 84050). All the raw chemicals were used without additional purification

Cobalt laurate was prepared by mixing equimolar aqueous solutions of cobalt acetate and sodium laurate. The pink precipitate was washed with de-ionized water and was dried at 50°C in order to remove the water excess. The cobalt laurate was characterized by thermogravimetric analysis (TGA) in air from room temperature to 600°C. The TGA showed a first mass loss of about 6% at 100°C followed by a second mass loss of 76-77 % in the temperature range from 200 to 450 °C. The total mass loss was between 82 and 83%. These mass losses are in a good agreement with a di-hydrated cobalt laurate (calculated mass losses : 7.3% for the loss of the two water molecules at 100°C and 83.7% for the total mass loss corresponding to the transformation of the di-hydrated cobalt laurate to Co_3O_4.

The cobalt laurate was dispersed in a sodium hydroxide solution of 1,2-butanediol. The concentration of cobalt was 8×10^{-2} mol.L^{-1} in all experiments. The NaOH concentration was 7.5×10^{-2} mol.L^{-1}. Ruthenium chloride was added in the medium to control the nucleation step. The ratio [Ru]/[Co] = 2.5% was fixed in all experiments. The suspension of cobalt laurate in the basic solution of butanediol containing the ruthenium chloride was heated up to 175 °C for 30 min under mechanical stirring in the range of 80 to 240 rpm. The solution turned into black indicating the cobalt reduction. Classic heating mantle was used as heating system. The temperature slope was fixed at 8 K.min^{-1}. Small and large scale experiments were performed in 100 mL and 1L of 1,2 butanediol leading to the formation of 0.47 g and 4.7 g of cobalt respectively.

The cobalt particles were characterized by transmission electron microscopy (TEM), using a 100kV Jeol JEM 1011. The cobalt particles were recovered by centrifugation, washed twice with absolute ethanol and once with chloroform. A drop of the colloidal solution of Co nanorods in chloroform was deposited on a carbon coated copper grid. Their mean diameter (d_m) and mean length (L_m) were measured from the image analysis on c.a. 200 rods using the ImageJ software[34] (image magnification 250k). X-ray diffraction (XRD) patterns were recorded on a PANalytical Empyrean diffractometer using the Co K$_\alpha$ radiation.

Assembly of Co NRs into dense anisotropic nanomaterials

Co NRs were washed in chloroform or in toluene prior to their alignment and after washing they were dispersed under sonication in chloroform. Dispersions containing approximately 1 g of powder in 10 mL of solvent were allowed to dry under air at room temperature in a homogenous magnetic field of 1T generated by an electro-magnet. The different assemblies are noted R_dAj for rods, exhibiting the mean diameter d, aligned following the procedure Aj. The alignments A1 and A3 correspond to rods washed in chloroform, A2 and A4 to rods washed in toluene. For A1 and A2 (standard procedures) three successive washings were realized, for A3 an extended washing was carried out. A4 corresponds to alignment of large scale samples for which the washing was limited in comparison to the standard samples.

The rod assemblies R_dAj were characterized by scanning electron microscopy (FEG-SEM) using a JEOL JSM 6700F. Thermogravimetric Analysis (TGA) was performed on a Mettler-Toledo balance in air and under H_2/Ar atmosphere.

The Small-Angle Neutron Scattering (SANS) experiments were carried out on the spectrometer PAXY at the Laboratoire Léon Brillouin.[35] The neutron wavelength was set at 5Å. The amount of magnetic material put in the beam was on the order of 10-20 mg ($5\times5\times0.1mm^3$).

The magnetic properties of the assemblies were characterized using a Quantum Design Physical Property Measurement System (PPMS) with the Vibrating Sample Magnetometer (VSM) configuration.

Magnetic measurements

The saturation magnetization values were measured on sample mass larger than 10 mg. *M(H)* loops were measured on small needles of dimensions c.a. $5\times 0.5\times 0.1$ mm with the applied field parallel to the needle long axis.

Volume fraction measurements

The assessment of the magnetic volume fraction, V_M, in the dense assemblies is necessary for the calculation of the energy product *(BH)max*. Assuming the absence of internal porosity in the assemblies, it is arguable that they consist of three components: the Co metal cores, a cobalt oxide shell around each cores, since the drying and alignment of the Co nanorods were carried out under air, and an outer ligand shell, i.e. the organic molecules remaining at the rod surface and occupying the inter-rod spacing. These organic molecules include the ligands and remaining solvent.

The volume fraction of the three components noted V_M, V_{CoO} and V_L, respectively were calculated from the mass fraction inferred from the VSM and TGA measurements.

The magnetic mass fraction was deduced from the saturation magnetization, M_S, of the samples measured by magnetometry:

$$\%w(Co_{metal}) = \frac{M_S}{M_{S\,cobalt}}$$

(Eq. 1)

with M_S expressed in emu·g^{-1} and $M_{S\,cobalt}$ = 160 emu.g^{-1}.

In order to determine the mass fraction of the Co oxide and the ligands in the NR assemblies, a sample of mass m_0 was heated in air at 700°C for 2 hours, in order to remove all the organics and to fully oxidize the cobalt core resulting in a mass gain $\Delta m_1 > 0$. After cooling at room temperature in the thermo-balance, the sample was then heated at 700°C under a mixture of H$_2$/Ar for 2 hours in order to reduce the cobalt oxide in metal cobalt resulting in a mass loss $\Delta m_2 < 0$. The final mass of the sample is m_3 and consists purely of metal Co.

The mass fraction of the total Co, $\%w(Co_{total})$, corresponding to the cobalt involved both in the metal core and in the oxide shell, was calculated from Eq. 2 (see an example in figure S2 of the supporting information).

$$\%w(Co_{total}) = \frac{m_3}{m_0} = 1 + \frac{\Delta m_1 + \Delta m_2}{m_0}$$

(Eq. 2)

This allow to deduce the mass fraction of the cobalt involved in the oxide shell :

$$\%w(Co^{II}) = \%w(Co_{total}) - \%w(Co_{metal})$$

(Eq. 3)

Assuming that the cobalt oxide at the surface of the cobalt rods is cobalt monoxide CoO, as previously reported,[36] its mass fraction can be calculated from the mass fraction of Co^{II} according to:

$$\%w(CoO) = \%w(Co^{II}) \times \frac{M_{Co} + M_O}{M_{Co}}$$

(Eq. 4)

with the molar weight M_{Co} = 58.9 g.mol^{-1} and M_O = 16 g.mol^{-1}.

Finally, the mass fraction of the ligands can be obtained by:

$$\%w(L) = 1 - \%w(Co_{metal}) - \%w(CoO)$$

(Eq. 5)

Then, assuming that the density of Co, CoO and ligands are similar to their bulk values, namely $\rho_{Co} = 8.9$, $\rho_{CoO} = 6.4$ and $\rho_L = 0.9$ g·cm^{-3} respectively, their volume fraction could be deduced as follows:

$$V_{Co} = \frac{\%w(Co_{metal})/\rho_{Co}}{[\%w(Co_{metal})/\rho_{Co}] + [\%w(CoO)/\rho_{CoO}] + [\%w(L)/\rho_L]} \qquad \text{(Eq. 6a)}$$

$$V_{CoO} = \frac{\%w(CoO)/\rho_{CoO}}{[\%w(Co_{metal})/\rho_{Co}] + [\%w(CoO)/\rho_{CoO}] + [\%w(L)/\rho_L]} \qquad \text{(Eq. 6b)}$$

$$V_L = \frac{\%w(L)/\rho_L}{[\%w(Co_{metal})/\rho_{Co}] + [\%w(CoO)/\rho_{CoO}] + [\%w(L)/\rho_L]} \qquad \text{(Eq. 6c)}$$

In the paper V_{Co} is noted V_M for magnetic volume fraction.

Assuming an ideal core-shell structure for the cobalt nanorods consisting of a metal cobalt cylinder core and a CoO shell, the thickness, e, of the CoO shell was calculated using:

$$e = \frac{d_m}{2} \times \left[1 - \sqrt{\frac{V_{Co}}{V_{Co} + V_{CoO}}} \right] \qquad \text{(Eq. 7)}$$

with d_m the external mean diameter of the rods determined by TEM.

Results and discussion

Nanorod alignment characterization

The cobalt nanorods prepared by the polyol process exhibited a mean diameter in the range 17-31 nm and a mean length in the range from 120 to 200 nm as observed on the transmission electron microscopy (TEM) images. Figure 1a shows a TEM image of representative rods exhibiting a mean diameter d_m = 22 nm. The TEM images of the different rods used in this study are given in the supporting information (Fig. S1). The thinner rods (d_m below 24 nm) have a regular diameter except at the tips while the larger ones exhibit irregularities along their length. The irregular rods with the larger mean diameters were obtained with the higher stirring rate (> 160 rpm). Decreasing the stirring rate to 80 rpm improved the rod morphology and decreased the mean diameter. X-ray diffraction shows that the cobalt rods crystallize with the hcp structure with the c axis parallel to the long axis as previously reported.[23] After being washed in organic solvents (chloroform or toluene) the nanorods were dispersed in chloroform. Large wafers of parallel assemblies of rods were obtained by drying the rod dispersions in a uniform magnetic field of 1 T (Fig. 1b). Although no additional polymer was used for the rod consolidation, the dried assemblies exhibit robustness along the axis parallel to the applied field during the solidification and flexibility perpendicular to it (Fig. 1c). Individual millimeter long needles with parallelepiped shape could be separated from these wafers for further characterizations (Fig. 1d). Scanning electron microscopy (SEM) of the needles showed smooth surfaces without any cracks (Fig. 1d) and dense alignments of parallel nanorods with their rod long axis parallel to the needle long axis (Fig. 1e).

Small angle neutron scattering (SANS) patterns were recorded on different rod assemblies. The patterns of the assemblies $R_{17}A1$ and $R_{17}A2$ are shown on figure 2 as examples. The alignment procedures of these two samples were different. In procedure A1, the rods were washed with chloroform, while in the procedure A2 they were washed with toluene (see experimental section). Very anisotropic scattering patterns are observed. The intensity scattered perpendicular to the rod direction measures the correlations between the rods: the better aligned, the higher the intensity. In the direction parallel to the rods the scattering is very low. From the 2D scattering patterns, it is possible to extract the scattered intensity parallel, $I_{//}$, and perpendicular to the rods, $I_{\perp}$. These two intensities are plotted on figures 2a and 2b. On the $I_{\perp}$ curves, a well-defined peak can be observed. It corresponds to the rod-rod distance in the correlation function. The intensity of this correlation peak is a measure of the quality of the alignment. It can be observed that depending on the alignment procedure (A1 or

A2) the quality of the alignment varies significantly. The q position of the correlation peak provides a measure of the mean center to center distance between rods, D_m, according to $q_{\perp max}$ = $2\pi/D_m$. For the assembly $R_{17}A1$ (figure 2a) the mean distance deduced from the correlation peaks at the wave vector $q_\perp$ =0.295 nm^{-1} is D_m= 21.3 nm. Considering the rod mean diameter d_m = 17.5 nm inferred from TEM images, the mean inter-rod distance is approximately h = D_m - d_m = 3.8 nm. This value is in agreement with an inter-rod spacing occupied by organic molecules like the laurate ions remaining at the surface of the Co NRs and solvent molecules trapped by capillary forces. The strong Van der Waals forces that apply at very small inter-rod distance explain the robustness of the assemblies. The Van der Waals energy between two parallel nanorods of radius R, length L and separated by a distance h can be estimated according to Eq. 8 (approximate expression valid for $h < R$).[37]

$$E_{VdW} = -\frac{A_H \times L \times R^{1/2}}{24 \times h^{3/2}}$$ (Eq. 8)

with A_H the Hamaker constant. Assuming A_H = - 50 k_BT for metallic cobalt dispersed in organic medium,[37] the Van der Waals energy between two rods in the assembly $R_{17}A1$ is estimated to E_{VdW} = -100 k_BT.

The better alignment in the assembly $R_{17}A1$ compared to $R_{17}A2$ observed on the SANS patterns is corroborated by the hysteresis cycle measurement which shows a squarer hysteresis loop for $R_{17}A1$ than for $R_{17}A2$ (Fig. 2c). The squareness SQ of the magnetization curve, measured with the field parallel to the rod long axis, was calculated as follow:

$$SQ = \frac{A}{H_C \times M_S}$$ (Eq. 9)

with A the area below the $M(H)$ loops in the second quadrant area, i.e. from $H = 0$ to $H = -Hc$, and $H_C \times M_S$ corresponding to the area of the ideal rectangle loop obtained for a fully parallel configuration. The SQ values of the $M(H)$ loops of the samples $R_{17}A1$ and $R_{17}A2$ were found equal to 0.86 and 0.75, in agreement with a sharper SANS peak recorded for the sample $R_{17}A1$. The squareness appears to be a more sensitive criterion than the remanence to saturation ratio, usually used, to describe the rod ordering. Indeed, despite the difference of alignment quality, fairly close values of M_R/M_S = 0.96 and 0.93 were found for the samples $R_{17}A1$ and $R_{17}A2$, respectively.

Magnetic measurement being more accessible than SANS, the squareness parameter can be routinely used to characterize the different assemblies, noted R_dAj, obtained with rods R_d

exhibiting the mean diameter d aligned following the procedure Aj (see experimental section). The squareness of several R_dAj samples is given in Tab. S1 of the supporting information. The best rod alignments in the dried assemblies were obtained with rods washed with chloroform ($SQ > 0.86$) rather than toluene ($SQ < 0.81$) (Tab. S1). We could observed experimentally that the rods R_{22} exhibiting the best shape homogeneity (low diameter dispersion, smooth surface) led to the best orientations. Successive chloroform washings also improved the quality of the alignment (Tab. S1).

Considering the absence of cracks in the needles and assuming no void inside, as suggested the SEM images, the volume fractions of the magnetic core (V_M), the oxide shell (V_{CoO}), and the remaining organic molecules (V_L) were calculated using the saturation magnetization values and the thermal analysis (see experimental section). The results for different rod assemblies are gathered in Table 1. The magnetic volume fraction V_M values were found in the range from 45 to 56%, the ligand volume fraction V_L in the range from 25 to 40% and the cobalt oxide volume fraction V_{CoO} was found in the range from 11 to 19% (Tab. 1). The thickness of the cobalt oxide shell, calculated using Eq. 7 (see experimental section), was found in the range from 1.1 to 1.4 nm for three samples (Tab. 1). The oxidation, which results from the air exposure of the Co NRs during the post-treatment process, remained rather limited, in good agreement with previous electron microscope observations on similar cobalt and cobalt-nickel nanorods.[36,38] However, one sample, R_{28}, suffered an additional undesired oxidation with an oxide shell thickness of about 1.8 nm. The thin oxide shell around the Co rods protects them from any further oxidation. When the rods were handled at room temperature in dry air the CoO shell thickness was found constant.
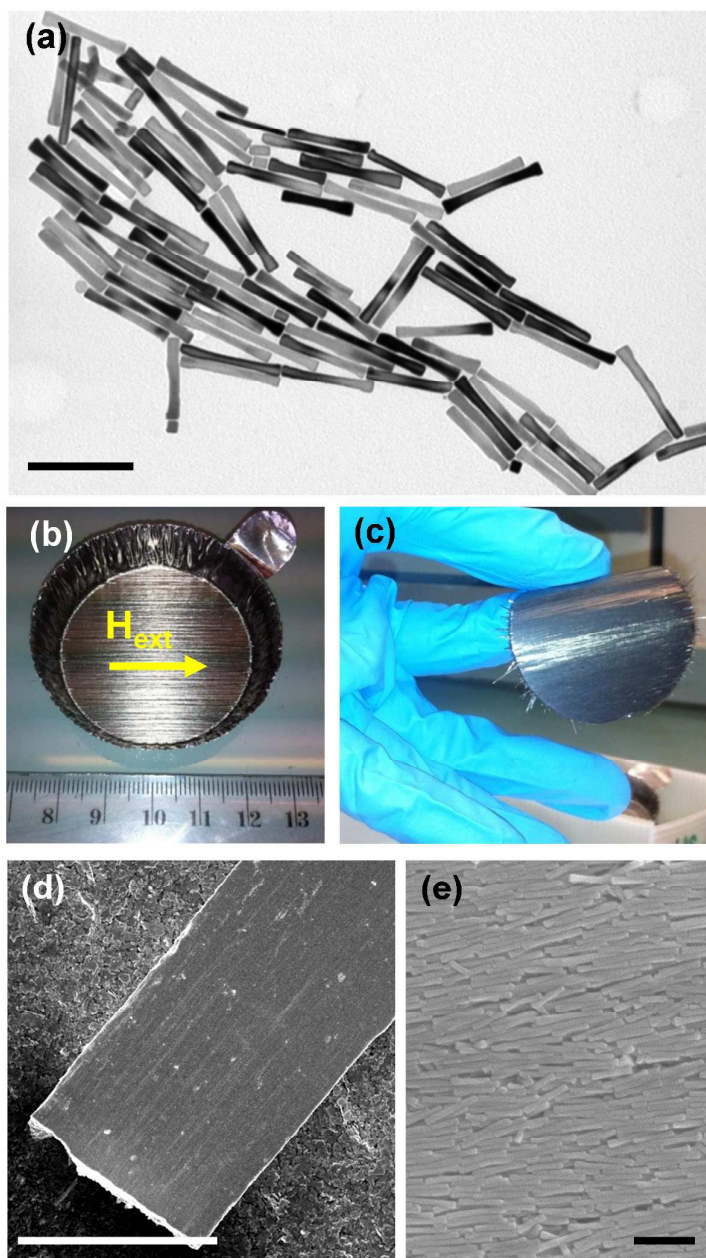
Fig. 1 (a) TEM image of cobalt nanorods prepared by the polyol process prior to their alignment ; (b) and (c) wafer of cobalt nanorods obtained by drying a suspension in chloroform under an external magnetic field of 1T; (d) SEM image of a millimeter size parallelepiped made of aligned cobalt nanorods; (e) SEM image of the surface of a parallelepiped. Scale bars denote (a) 200 nm, (d) 100 μm and (e) 200 nm.
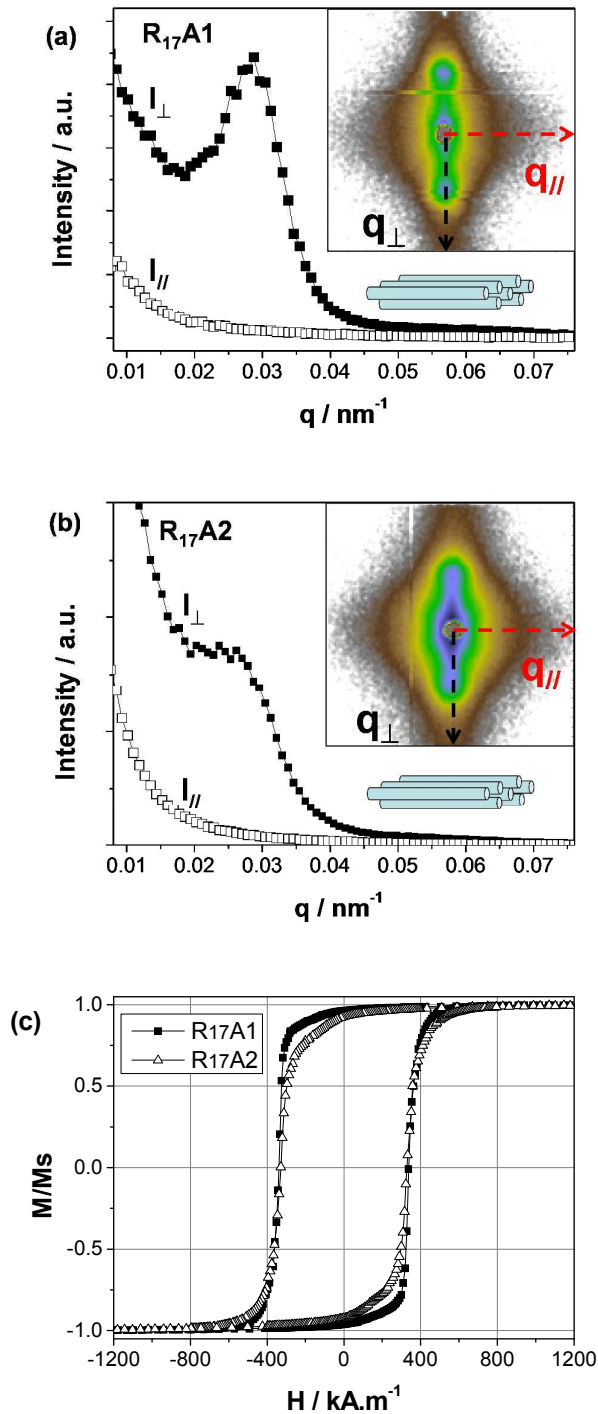
Fig. 2 (a) and (b) Small angle neutron intensity profile scattered by two cobalt nanorod assemblies ($R_{17}A1$ and $R_{17}A2$), perpendicular (black square) and parallel (open square) to the rod alignment. *Inset*: corresponding 2D SANS pattern; (c) Magnetization curves in parallel configuration of the assemblies $R_{17}A1$ (black square) and $R_{17}A2$ (open triangle).

Table 1 Summary of the morphological, chemical and magnetic properties of densely packed assemblies of cobalt nanorods: d_m, mean diameter and L_m, mean length of the rods; V_M is the magnetic volume fraction, V_{CoO} the cobalt oxide volume fraction and V_L the ligand volume fraction ; e is the cobalt oxide shell thickness around the rods calculated from Eq. 7; M_R/M_S is the remanence to saturation ratio and μ_0H_C the coercivity; $B_R = V_M \times B_{Co\ bulk}$ is the remanence of the B(H) loops and $(BH)_{max}$ the energy product; SQ is the squareness of the M(H) loops, α is the slope of the model curve calculated from Eq. 11 and $B_R/2(1+\alpha)$ is the critical magnetic field of Eq. 13. The sample noted $R_{dm}Aj$ corresponds to the washing protocol and alignment Aj of the rods R of mean diameter d_m.

Sample	d_m/L_m	V_M	V_{CoO}	V_L	e (CoO)	M_R/M_S	μ_0H_C	B_R	$(BH)_{max.}$	SQ	α	$\dfrac{B_R}{2(1+\alpha)}$
	(nm)	(%)	(%)	(%)	(nm)		(T)	(T)	(kJ.m^{-3})			(T)
R$_{22}$A1	22/166	48.7	14.0	37.3	1.3	0.98	0.436	0.85	125	0.93	0.27	0.334
R$_{22}$A2	22/166	47.9	15.2	36.9	1.4	0.92	0.451	0.79	92	0.79	0.74	0.228
R$_{22}$A3	22/166	54.4	12.0	33.6	1.1	0.99	0.465	0.96	165	0.96	0.165	0.412
R$_{24}$A1	24/190	48.7	11.0	40.3	1.2	0.92	0.410	0.80	82	0.74	1.02	0.198
R$_{28}$A2	28/190	55.1	19.3	25.6	1.9	0.96	0.345	0.95	106	0.81	1.05	0.232
R$_{28}$A4	28/190	48.8	15.6	35.6	1.8	0.89	0.363	0.78	51	0.57	1.85	0.137
R$_{31}$A4	31/190	56.8	11.6	31 .6	1.4	0.94	0.339	0.95	81.5	0.69	1.735	0.174

Magnetic properties and (BH)$_{max}$ assessment

The magnetization curves *M(H)* of the different assemblies were measured at room temperature. In table 1 are given the main magnetic properties, remanence to saturation ratio (M_R/M_S), squareness (*SQ*), coercivity (H_C) and induction remanence (B_R), of several assemblies. The H_C values were found in the range from 270 to 360 kA/m ($\mu_0 H_C$ from 0.34 to 0.47 T). All the rods of this study exhibit an aspect ratio comprised between 6 and 8. As expected the highest H_C values were obtained with the thinnest nanorods in agreement with previous experimental studies and micro-magnetic modelling.[39]

The remanence to saturation ratio was comprised between M_R/M_S = 0.89 and 0.99, values above 0.9 are generally considered as a criterion of a good alignment. Nevertheless, the squareness was observed to vary in a broader range with values comprised between 0.57 and 0.96 (Tab. 1). It is noteworthy that the highest value *SQ* = 0.96, obtained for sample R$_{22}$A4, corresponds to a nearly perfect alignment and is, as far as we know, the best value for an anisotropic particle assembly.

The energy product *(BH)$_{max}$* is the figure of merit of a magnet performance. The working point is the value of the *B(H)* loop corresponding to the maximum of the *B×H* product. The determination of the magnetic volume fraction (V_M) within the assemblies allowed to plot the *B(H)* loops and to assess the *(BH)$_{max}$*. On figure 3 are plotted the second quadrant of the *B(H)* loop and the *B×H* product over the second quadrant of a representative sample (R$_{22}$A1). An energy product of 125 kJ.m^{-3} was determined for this assembly that exhibited a magnetic volume fraction V_M = 48.7 % and a *M(H)* loop squareness *SQ* = 0.93. The *(BH)$_{max}$* values calculated following the same method for the different assemblies were found in the range from 50 to 165 kJ.m^{-3} (Tab. 2) depending on the magnetic volume fraction and on the quality of the alignment.

On figure 4 are plotted the *B(H)* curves of three assemblies exhibiting the same magnetic volume fraction (~48.8%) but prepared with different rod batches. The squareness of the *M(H)* loops of these samples varied from 0.57 to 0.93 showing strong differences in the quality of the rod alignment. The opening of the hysteresis loop has for consequence to increase the energy product from 51 to 125 kJ.m^{-3} (Fig. 5b).

The other parameter that has a strong influence on the value of the energy product is the magnetic volume fraction within the assembly. On figure 5 are plotted the *B(H)* curves of two samples prepared with the same rods and exhibiting similar squareness (0.93 and 0.96).

Increasing the magnetic volume fraction from 48.7% to 54.4 % increases the $(BH)_{max}$ from 125 to 165 kJ.m^{-3}.

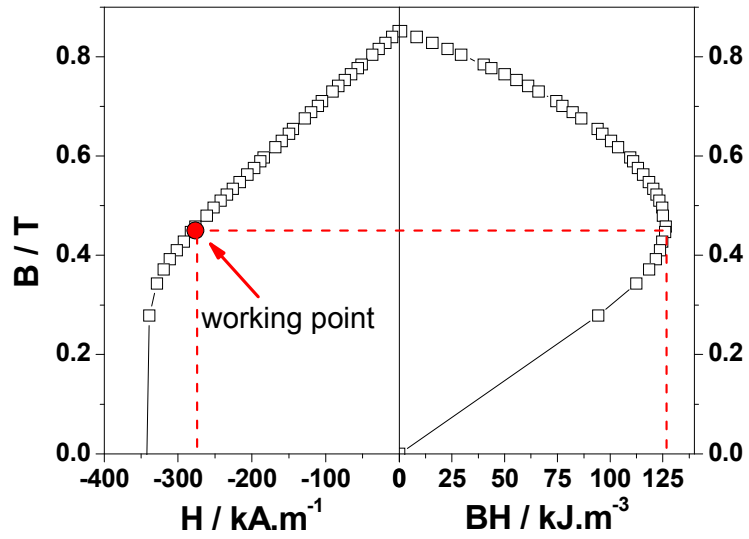**Fig. 3** Second quadrant of the B-H loop and energy product $(BH)_{max}$ = 125 kJ.m^{-3} of the Co NR assembly R$_{22}$A1.
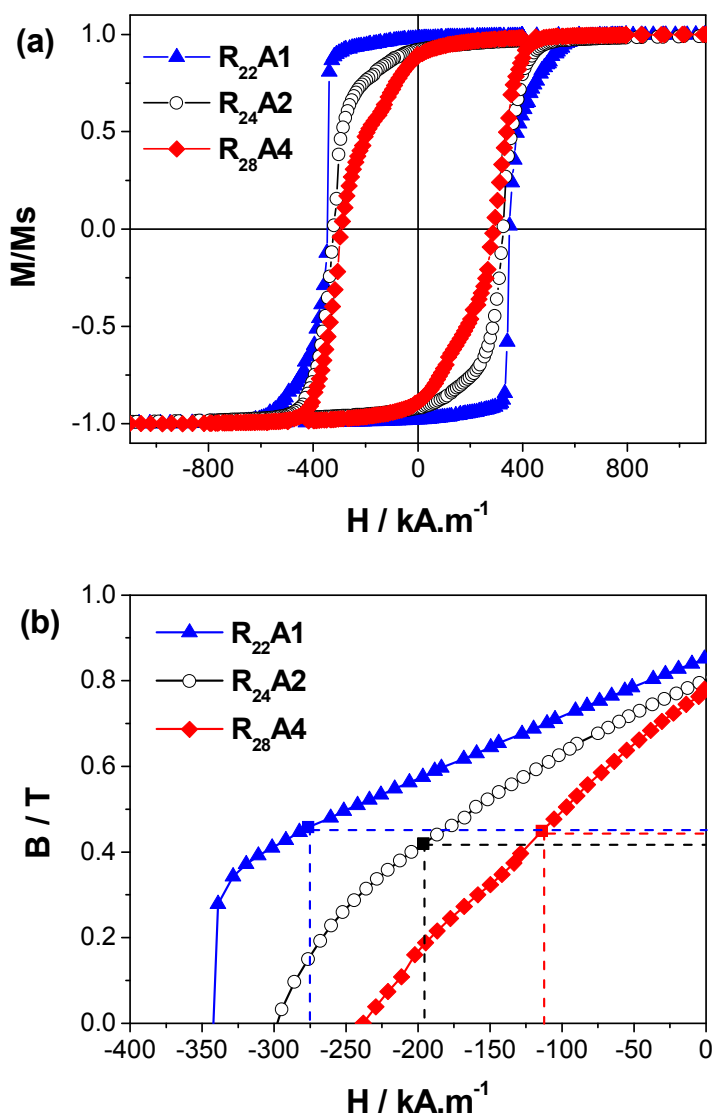
Fig. 4 Normalized *M(H)* loops (a) and second quadrant of the corresponding *B(H)* loops (b) of three rod alignments exhibiting the same magnetic volume fraction: Sample $R_{22}A1$ (blue triangle): V_M = 48.7%, *SQ* = 0.93, $(BH)_{max}$ = 125 kJ.m^{-3} ; sample $R_{24}A2$ (black circle): V_M = 48.7%, *SQ* = 0.74, $(BH)_{max}$ = 82.5 kJ.m^{-3}; sample $R_{28}A4$ (red diamond): V_M = 48.8%, *SQ* = 0.57, $(BH)_{max}$ = 51 kJ.m^{-3}.
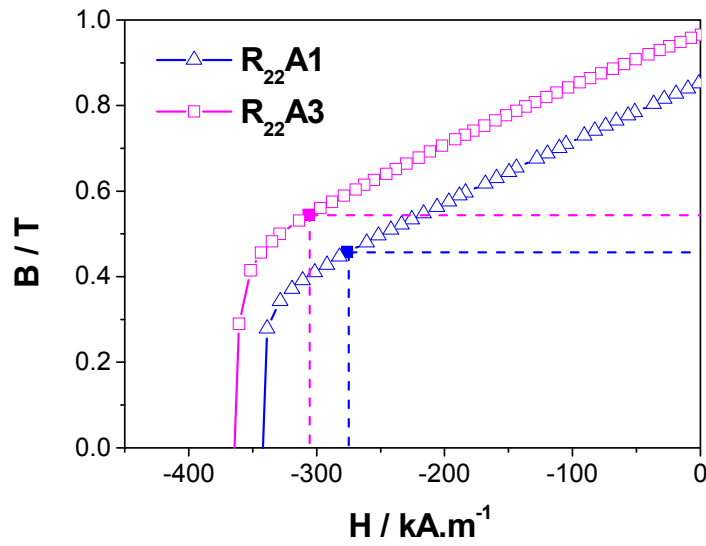
Fig. 5 Second quadrant of the *B(H)* loops and working points of the assemblies $R_{22}A1$ and $R_{22}A3$ prepared with cobalt nanorods of mean diameter d_m = 22 nm. Sample $R_{22}A1$ (blue triangle): V_M = 48.7%, SQ = 0.93, *(BH)$_{max}$* = 125 kJ.m^{-3} ; sample $R_{22}A3$ (magenta square): V_M = 54.4%, SQ = 0.96, *(BH)$_{max}$* = 165 kJ.m^{-3}.

17

Discussion

The results gathered in Table 1 show that the highest *(BH)$_{max}$* was obtained for the sample that combined a high magnetic volume fraction and a squared *M(H)* loop with a very large *SQ*, which indicates a very good alignment of the nanorods.

The energy product of a sample exhibiting a perfectly square magnetization curve is:[31]

$$(BH)_{max} = B_R^2/4\mu_0 \qquad\qquad \text{if } \mu_0 H_C \geq B_R/2 \qquad\qquad \text{(Eq. 10a)}$$

$$(BH)_{max} = H_C(B_R - \mu_0 H_C) \qquad\qquad \text{if } \mu_0 H_C \leq B_R/2 \qquad\qquad \text{(Eq. 10b)}$$

In order to describe the effect of partial order in the rod assembly we consider schematically a linear variation of the magnetization in the second quadrant of the *M(H)* loop as follows:

$$M = M_R + \alpha H$$

with α the slope of the *M(H)* loop at remanence (Fig. 6). The parameter α can be deduced from the squareness defined above by:

$$\alpha = \frac{2M_R(1-SQ)}{H_C} \qquad\qquad \text{(Eq. 11)}$$

α is comprised between 0 and M_R/H_C, α = 0 for a perfect parallel orientation and α > 0 characterizing a degree of disorder in the assembly.

For such *M(H)* loops the energy product can be written as:

$$(BH)_{max} = \frac{B_R^2}{4\mu_0(1+\alpha)} \qquad\qquad \text{if } \mu_0 H_C \geq \frac{B_R}{2(1+\alpha)} \qquad\qquad \text{(Eq. 12a)}$$

$$(BH)_{max} = H_C[B_R - \mu_0(1+\alpha)H_C] \qquad\qquad \text{if } \mu_0 H_C \leq \frac{B_R}{2(1+\alpha)} \qquad\qquad \text{(Eq. 12b)}$$

For a magnetic volume fraction V_M, in the assembly the remanence is $B_R = V_M \times B_{Cobulk}$ (with $B_{Co\ bulk}$ = 1.79 T). So, in the case of a coercivity higher than the critical field $\dfrac{B_R}{2(1+\alpha)}$ the energy product becomes:

$$(BH)_{max} = \frac{B_{Cobulk}^2}{4\mu_0} \times \left[\frac{V_M^2}{(1+\alpha)}\right] \qquad\qquad \text{(Eq. 13)}$$

The magnetic field and induction of the working point are:

$$H = -\frac{B_R}{2\mu_0(1+\alpha)} \qquad \text{and} \qquad B = \frac{B_R}{2} \qquad\qquad \text{(Eq. 14)}$$
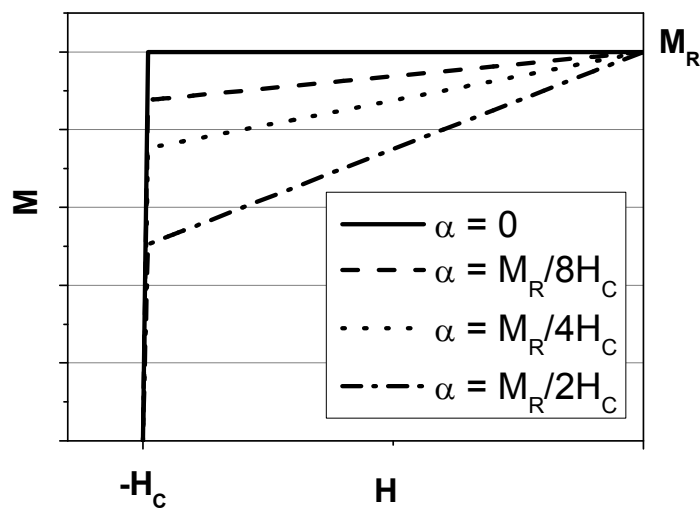
Fig. 6 Second quadrant of model M(H) loops with $M = M_R + \alpha \times H$ for different value of the slope α. The squareness of the four loops is 1, 0.9375, 0.875 and 0.75.

In table 1 are given the α values calculated from the squareness following Eq. 11. All the samples studied exhibited coercivity higher than the critical field $B_R/2(1+\alpha)$ (Tab. 2) showing that the experimental data have to be compared with the formula of Eqs. 13 and 14. According to Eq. 13 the energy product varies as a quadratic function of the magnetic volume fraction. It describes well the important improvement of $(BH)_{max}$ observed on figure 5 when the volume fraction was increased from 48.7% in the sample $R_{22}A1$ to 54.4% in the sample $R_{22}A3$ (Tab. 1). Such dependence on the magnetic volume fraction explains also why, despite a poor squareness, the assemblies prepared with the thicker rods ($R_{31}A4$ and $R_{28}A2$ in table 1) exhibit a rather good $(BH)_{max}$.

Eq. 13 predicts also that the energy product varies as an inverse function of the slope of the $M(H)$ loop. On figure 4 are compared the samples $R_{22}A1$, $R_{24}A2$ and $R_{28}A4$ that contained almost the same magnetic volume fraction (Tab. 1) and that exhibited $M(H)$ loop with different squareness, 0.93, 0.74 and 0.57, respectively (Tab.2). For these three samples the B value of the working point is found almost constant (Fig. 4b) and close to $B_R/2$ as predicted by Eq. 14. The decreasing of the $(BH)_{max}$ value is only due to the decreasing of the H value of the working point (Fig. 4b) as predicted by Eq. 14. The α values corresponding to the model

M(H) curves calculated according to Eq. 11 were found equal to 0.27, 1 and 1.85 for the samples $R_{22}A1$, $R_{24}A2$ and $R_{28}A4$, respectively (Tab. 2). The energy product calculated with these values according to Eq. 13 were found equal to 53, 75 and 119 kJ.m^{-3}, very close to the experimental energy products (51, 82 and 125 kJ.m^{-3}). *(BH)$_{max}$* increases linearly with the ratio $V_M^2/(1+\alpha)$ (Fig. 7). The slope of the linear fit is 670 kJ.m^{-3}, very close to $B_{Cobulk}^2/4\mu_0 =$ 638 kJ.m^{-3} as expected from Eq. 13, showing that our simple model applies quite well.
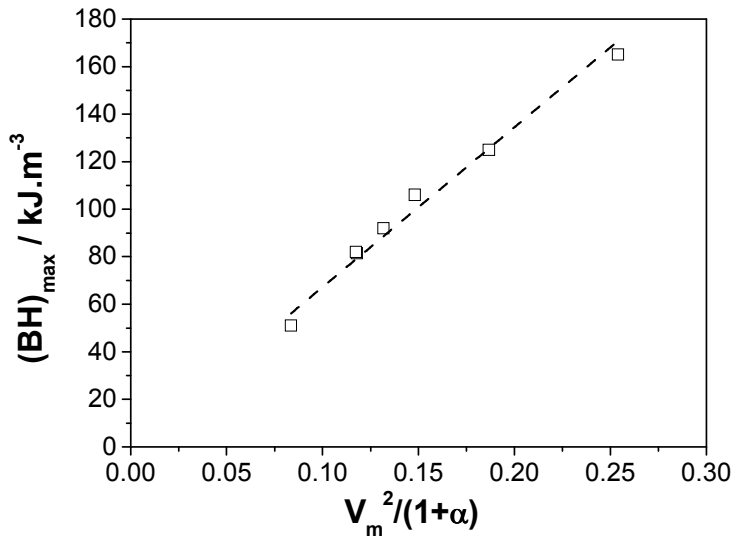

Fig. 7 Experimental energy product vs $V_M^2/(1+\alpha)$ with V_M the magnetic volume fraction and α the slope of the model *M(H)* curve at remanence (dashed line: linear fit).

Magnet performance optimization

The *(BH)$_{max}$* value of 165 kJ.m^{-3} obtained with a dense assembly of parallel cobalt nanorods is higher than the *(BH)$_{max}$* of classical ferrites and AlNiCo magnets and comes close to the energy product of bonded NdFeB magnets.[40] This is the first proof of concept that such dense arrays can compete in the magnet panorama. The best assembly described in this paper exhibited a squareness *SQ* = 0.96 showing that there is quasi no more room to improve the

alignment quality. So, in order to increase the *(BH)$_{max}$* the next goal is to increase the magnetic volume fraction. On figure 8 are plotted the magnetic volume fraction and the energy product of perfect hexagonal arrays of nanorods as a function of the rod diameter for an inter-rod distance fixed at 3.5 nm. Non-oxidized and oxidized rods with a CoO shell thickness of 1.2 nm, were considered. For a given ligand amount in the assemblies the magnetic volume fraction increases when the rod diameter increases explaining why it is easier to reach higher volume fraction with thicker rods. Nevertheless, even if a significant increase of *(BH)$_{max}$* is expected, an increase of the rod diameter must be discarded for permanent magnet applications due to the decrease of coercivity which may potentially drop below the critical field (Eq. 12). Another way to increase the magnetic volume fraction would be to avoid the rod oxidation. For rod diameter in the range from 10 to 20 nm the oxidation dramatically decreases the magnetic volume fraction (Fig. 8a). Magnetic volume fraction of 60% and 65% are expected for non-oxidized rods of diameter 15 and 20 nm, respectively, while only 42 and 51% are expected for oxidized ones (Fig. 8a). Finally, a significant increase of volume fraction could also be reached by lowering the organic amount. With non-oxidized rods separated by only a ligand shell of only 2 nm the magnetic volume fraction could reach 70 and 75% for 15 and 20 nm rods (Fig. 8a). [‡] The effect of oxidation and inter-rod spacing on the energy product is even more important on the energy product value since it varies as the square of the magnetic volume fraction (Fig. 8b). According to Eq. 13 magnetic volume fraction in the range from 60 to 75 % could lead to *(BH)$_{max}$* values from 230 to 360 kJ.m^{-3} providing a perfectly square hysteresis loop and from 180 to 280 kJ.m^{-3} for a more realistic squareness $SQ = 0.93$ ($\alpha = 0.27$). Such energy product would require a coercivity $\mu_0 H_C$ higher than $B_R/2$, i.e. above 0.54 T and 0.67 T for a magnetic volume fraction of 60 % and 75 % respectively. Such values of coercivity have already been obtained with thin cobalt nanorods,[22,39] showing that there is still room to improve the *(BH)$_{max}$* of Co NRs assemblies.
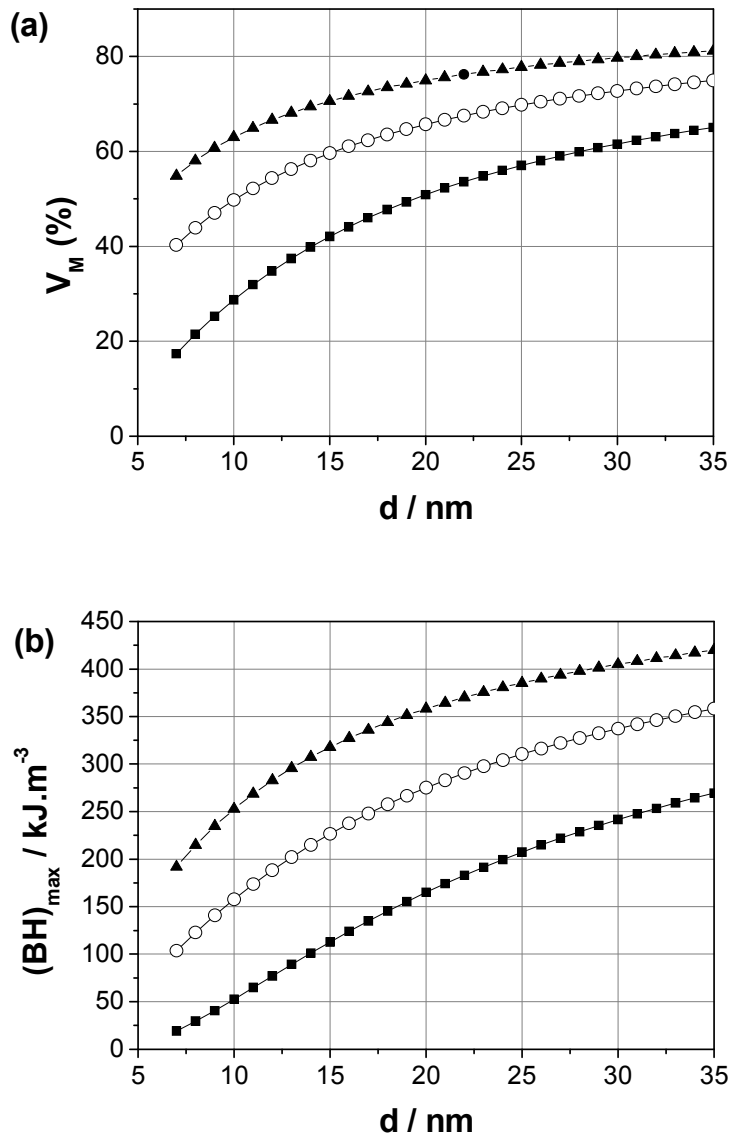
(a)

(b)

Fig. 8 Magnetic volume fraction (a) and energy product (b) of perfectly aligned hexagonal arrays of cobalt nanorods of mean diameter d separated by a ligand shell of 3.5 nm, oxidized rods with a CoO shell thickness of 1.2 nm (full square) and non-oxidized rods (open circle); non oxidized rods separated by a ligand shell of 2 nm (full triangle).

Conclusions

This is the first time that the energy products of nanorod assemblies have been assessed experimentally. Good alignment and high magnetic volume fraction are the two requirements to obtain important *(BH)$_{max}$*. We have shown that cobalt nanorods synthesized by the polyol process, washed and re-dispersed in chloroform are very well suited to get highly packed assemblies with a nearly perfect rod alignment. Very homogeneous Co NRs (low standard deviation on the diameter, no roughness) leads to *M(H)* loop squareness in the range from 0.93 to 0.96, indicative of a very good parallel order, while magnetic volume fractions were found in the range from 45 to 55%. The highest volume fraction combined with a nearly perfect alignement (SQ = 0.96) allowed to reach a *(BH)$_{max}$* of 165 kJ.m^{-3}, a value much higher than the energy product of barium ferrite and AlNiCo magnets. The road map for a *(BH)$_{max}$* improvement is now clear. The next goal will be to increase the magnetic volume fraction by avoiding the rod oxidation and by decreasing the ligand amount in the final material, while maintaining a rod mean diameter below 15-20 nm in order to keep a high coercivity. A *(BH)$_{max}$* increasing of a factor 1.5 is a reasonable goal for a near future, opening perspective for rare earth free permanent magnets of 250 kJ.m^{-3} competing with bounded SmCo and NdFeB. Furthermore, the bottom-up approach should allow to down-size magnets to the millimeter and submillimeter scale and open perspectives for an integration into micro-devices.

† **Electronic supplementary information (ESI) :** Transmission electron microscopy images of the cobalt nanorods ; Thermogravimetric analysis of a dense array of cobalt nanorods ; Table S1 Details on the rod washing and alignment procedure

Graphical abstract

24
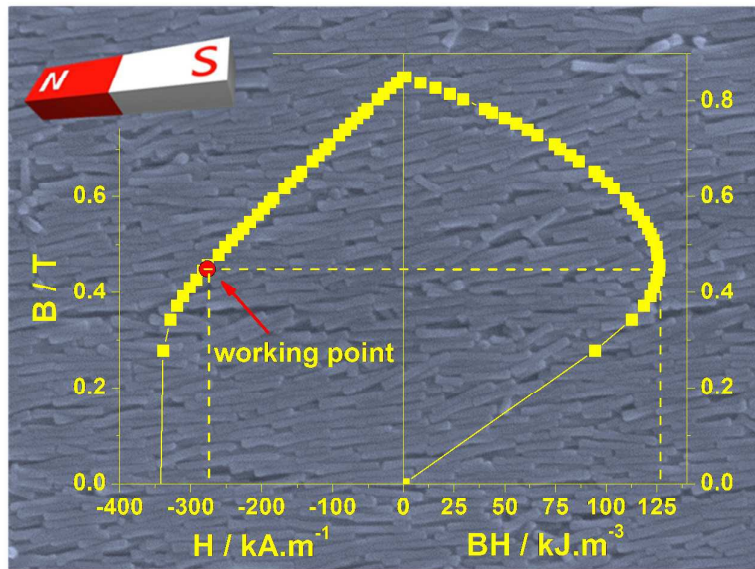
Notes and References

‡ Note that spacing between the rods is necessary to avoid a magnetic exchange and the loss of the shape anisotropy.

1   O. Gutfleisch, M. A. Willard, E. Brück, C. H. Chen, S. G. Sankar, and J. P. Liu, *Adv. Mater.,* 2011, **23**, 821.

2   J. M. D. Coey, *Scripta Materialia,* 2012, **67**, 524.

3   L. H. Lewis and F. Jiménez-Villacorta, *Metallurgical and Materials Transactions A,* 2013, **44**, 2.

4   J. M. D. Coey, *J. Phys.: Condens. Matter,* 2014, **26**, 064211.

5   (a) L. H. Lewis, A. Mubarok, E. Poirier, N. Bordeaux, P. Manchanda, A. Kashyap, R. Skomski, J. Goldstein, F. E. Pinkerton, R. K. Mishra, R. C. Kubic Jr, K. Barmak, *J. Phys.: Condens. Matter,* 2014, **26**, 064213;
    (b) Y. Hayashi, S. Gotou, M. Mizuguchi, M. Kotsugi, Y. Kitou, E. Okuno, K. Takanashi, *J. Magn. Soc. Jpn*, 2013, **37**, 198.
    (c) A. Makino, P. Sharma, K. Sato, A. Takeuchi, Y. Zhang, K. Takenaka, *Sci. Report*, 2015, **5**, 16 627.

6   M. D. Kuz'min, K. P. Skokov, H. Jian, I. Radulov, O. Gutfleisch, *J. Phys.: Condens. Matter,* 2014, **26**, 064205.

7   V.G. Harris, Y. Chen, A. Yang, S. Yoon, Z. Chen, A.L. Geiler, J. Gao, C. N. Chinnasamy, L. H. Lewis, C. Vittoria, E. E. Carpenter, K. J. Carroll, R. Goswami, M A Willard, L. Kurihara, M Gjoka, O. Kalogirou, *J. Phys. D: Appl. Phys.,* 2010, **43**, 165003.

8   K. J. Carroll, Z. J. Huba, S. R. Spurgeon, M. Qian, S. N. Khanna, D. M. Hudgins, M. L. Taheri, E. E. Carpenter, *Appl. Phys. Lett.,* 2012, **101**, 012409.

9   N. Poudyal and J. P. Liu, *J. Phys. D: Appl. Phys.,* 2013, **46**, 043001.

10 R. Skomski , P. Manchanda , P. Kumar , B. Balamurugan , A. Kashyap , D. J. Sellmyer, *IEEE Trans. Magn.* 2013, **49**, 3215.

11 D. P. Arnold, *IEEE Trans. Magn.* **2007**, *43*, 3940.

12 B. Balasubramanian, B. Das , R. Skomski , W. Y. Zhang , D. J. Sellmyer, *Adv. Mater.,* 2013, **25**, 6090.

13 B. Balasubramanian, P. Mukherjee, R. Skomski, P. Manchanda, B. Das, D. J. Sellmyer, *Sci. Rep.,* 2014, **4**, 6265.

14 J. S. Jiang and S. D. Bader, *J. Phys.: Condens. Matter,* 2014, **26**, 064214.

15 M. Vazquez, *Magnetic Nano- and Microwires, Design, Synthesis, Properties and Applications*, 1ˢᵗ Edition, Woodhead Publishing 2015.

16 K. Gandha, P. Tsai, G. Chaubey, N. Poudyal, K. Elkins, J. Cui, J. Ping Liu, *Nanotechnology,* 2015, **26**, 075601.

17 Y. Soumare, A. Dakhlaoui-Omrani, F. Schoenstein, S. Mercone, G. Viau, N. Jouini, *Solid State Commun.,* 2011, **151**, 284.

18 Y. Soumare, J.-Y. Piquemal, T. Maurer, F. Ott, G. Chaboussant, A. Falqui, G. Viau, *J. Mater. Chem.,* 2008, **18**, 5696.

19 Y. Soumare, C. Garcia, T. Maurer, G. Chaboussant, F. Ott, F. Fiévet, J.-Y. Piquemal, G. Viau, *Adv. Funct. Mater,.* 2009, **19**, 1971.

20 K. Soulantica, F.Wetz, J.Maynadié, A.Falqui, R.P.Tan, T.Blon, B.Chaudret, M. Respaud, *Appl. Phys. Lett.,* 2009, **95**, 152504.

21 N. Liakakos, T.Blon, C. Achkar, V. Vilar, B. Cormary, R. P. Tan, O. Benamara, G. Chaboussant, F. Ott, B. Warot-Fonrose, E. Snoeck, B. Chaudret, K. Soulantica, M. Respaud, *NanoLett.,* 2014, **14**, 3481.

22 K. Gandha, K. Elkins, N. Poudyal, X. Liu, J.P. Liu, *Sci. Rep.,* 2014, **4**, 5345.

23 K. Aït Atmane, C. Michel, J.-Y. Piquemal, P. Sautet, P. Beaunier, M. Giraud, M. Sicard, S. Nowak, R. Losno, G. Viau, *Nanoscale,* 2014, **6**, 2682.

24 N. Ouar, S. Farhat, S. Mercone, F. Zighem, F. Schoenstein, N. Jouini, I. Hinkov, G. Wang, C. Ricolleau, *AIChE Journal*, 2015, **61**, 304.

25 O. Riou, B. Lonetti, P. Davidson, R. P. Tan, B. Cormary, A.-F. Mingotaud, E. Di Cola, M. Respaud, B. Chaudret, K. Soulantica, M. Mauzac, *J. Phys. Chem. B,* **2014**, *118*, 3218.

26 M. Ibrahim, C. Garcia, K. Aït Atmane, E. Berrichi, L.-M. Lacroix, A. Zwick, B. Warot-Fonrose, S. Lachaize, J.-Y. Piquemal, G. Viau, J. Phys. Chem. C, 2013, 117, 15808.

27 K. Aït Atmane, F. Zighem, Y. Soumare, M. Ibrahim, R.Boubekri, T. Maurer, J. Margueritat, J. –Y. Piquemal, F. Ott, G. Chaboussant, F. Schoenstein, N. Jouini, G. Viau, *J. Solid State Chem.,* 2013, **197**, 297.

28 F. Ott, T. Maurer, G. Chaboussant, Y. Soumare, J.-Y. Piquemal, G. Viau, *J. Appl. Phys.,* 2009, **105**, 013915.

29 I. Panagiotopoulos, W. Fang, K. Ait-Atmane, J.-Y. Piquemal, G. Viau, F. Dalmas, F. Boué, F. Ott, *J. Appl. Phys.,* 2013, **114**, 233909.

30 I. Panagiotopoulos, W. Fang, F. Ott, F. Boué, K. Aït-Atmane, J.-Y. Piquemal, G. Viau, *J. Appl. Phys.* 2013, **114**, 143902.

31   P. Toson, A. Asali, W. Wallisch, G. Zickler, J. Fidler, *IEEE Trans. Magn.*, 2015, **51**, 7400104.

32   T. Maurer, F. Ott, G. Chaboussant, Y. Soumare, J.-Y. Piquemal, G. Viau, *Appl. Phys. Lett.,* 2007, **91**, 172501.

33   B. Balamurugan, B. Das, V. R. Shah, R. Skomski, X. Z. Li, D. J. Sellmyer, *Appl. Phys. Lett.,* 2012, **101**, 122407.

34   W.S. Rasband, *ImageJ*, U. S. National Institutes of Health, Bethesda, Maryland, USA, http://rsb.info.nih.gov/ij/, 1997-2007.

35   http://www-llb.cea.fr/spectros/pdf/paxy-llb.pdf

36   T. Maurer, F. Zighem, F. Ott, G. Chaboussant, G. André, Y. Soumare, J.- Y. Piquemal, G. Viau, C. Gatel, *Phys. Rev. B,* 2009, **80**, 064427.

37   J. N. Israelachvili, Intermolecular and Surface Forces, Academic Press, 1985.

38   S. Liébana-Viñas, U. Wiedwald, A. Elsukova, J. Perl, B. Zingsem, A. S. Semisalova, V. Salgueiriño, M. Spasova, M. Farle, *Chem. Mater.,* 2015, **27**, 4015.

39   M. Pousthomis, E. Anagnostopoulou, I. Panagiotopoulos, R. Boubekri, W. Fang, F. Ott, K. Aït Atmane, J.-Y. Piquemal, L.-M. Lacroix, G. Viau, *Nano Research,* 2015*,* **8**, 2231.

40   J. M. D. Coey, *IEEE Trans. Magn.,* 2011, **47**, 4671.